Room-Temperature Manipulation of Spin Texture in a Dirac Semimetal

An-Qi Wang,[1,2,†] Peng-Zhan Xiang,[1,†] Xing-Guo Ye,[1,†] Wen-Zhuang Zheng,[1] Dapeng Yu,[3] and Zhi-Min Liao[1,4,*]

[1]*State Key Laboratory for Mesoscopic Physics and Frontiers Science Center for Nano-optoelectronics, School of Physics, Peking University, Beijing 100871, China*

[2]*Academy for Advanced Interdisciplinary Studies, Peking University, Beijing 100871, China*

[3]*Institute for Quantum Science and Engineering and Department of Physics, Southern University of Science and Technology, Shenzhen 518055, China*

[4]*Beijing Key Laboratory of Quantum Devices, Peking University, Beijing 100871, China*

Charge-current-induced spin-polarized current, via spin-momentum-locked states, is very attractive for spintronics. The orientation of spin polarization caused by an electric field depends on the helicity of the spin texture, which is normally opposite for typical topological surface states and Rashba states. Here, we report the manipulation of the two opposite spin textures in Dirac semimetal Cd_3As_2 nanoplates. Spin-polarized transport signals originated from topological surface states are detected through Hall-bar-like Co electrodes, showing a maximum at the Dirac point and robustness up to room temperature. By comparison, opposite helicity of the spin texture is measured by applying Co electrodes across the whole nanoplate. Furthermore, it is found that the opposite spin texture is only localized underneath the electrodes, and the spin texture of topological surface states can be singled out by a nonlocal device geometry. The results show that the clockwise and counterclockwise spin textures can be achieved simultaneously in a single Dirac semimetal device by patterning metal electrodes with different configurations, which are promising for future spintronic applications.

I. INTRODUCTION

Three-dimensional topological insulators possess topologically nontrivial surface states protected by time-reversal symmetry [1]. One of the most striking properties of TI surface states is spin-momentum locking [2], where the in-plane spin is locked perpendicularly to the electron momentum [3], that is, a helical spin texture [4]. Thus, a charge current would induce a spin-polarized current, which is promising for spintronic applications [5]. Similarly, topological semimetals (TSMs) [6] are also believed to possess topological surface states, that is, Fermi arcs [7], which connect the surface projection of bulk Weyl nodes with opposite chirality [6]. The Fermi arc surface states of topological semimetals are believed to have similar spin textures to those of the TI surface states [8–12]. Despite the conductive bulk, the large spin polarization ratio [11] and highly efficient gate tunability [12] make the TSMs a potential platform for high-performance spintronic applications [11–15]. Moreover, TSMs have ultrahigh mobility

and a long mean free path [14], which is promising for nonlocal spin filters.

Extensive studies have been carried out on the current-induced spin polarization in topological insulators [3,4,16–24] via ferromagnetic (FM) electrodes. Although the topological surface states induced spin polarization has been experimentally confirmed, it still remains a puzzle that the observed effective spin polarization (approximately 1%) in topological insulators [16,18] is much lower than theoretical expectation (approximately 50%) [25]. Furthermore, the observed spin texture is even opposite to the one expected from topological surface states [3,4]. The existence of the Rashba effect in topological materials gives a possible origin of the observed opposite spin texture [4,16]. The formation of a large Rashba spin splitting usually requires a strong interfacial electric field, which could occur at the interfaces between topological materials and FM metals [4,26]. Such an interface is crucial for spin injection [27] and spin-orbit torque (SOT) induced magnetization switching [28–32]. Nevertheless, the coexistence of the two counterhelical spin textures is harmful for the formation of spin polarization [4]. Therefore, it is highly desirable for precise control over the spin contributions from topological surface states and Rashba states.

---

*liaozm@pku.edu.cn

[†]These authors contributed equally to this work.

054044-1

Here, we report the manipulation of the opposite spin textures in Dirac semimetal Cd_3As_2 nanoplates by designing specific FM electrode patterns. We fabricate two types of FM electrodes in a single device, that is, Co electrodes contacting one side of the sample (i.e., Hall-type) and the ones across the whole sample. The observed spin-momentum locking via Hall-type Co electrodes is consistent with the topological surface states, which are robust up to room temperature. On the contrary, the opposite spin texture is observed via the Co electrode across the sample. The opposite spin texture can be well understood by considering the interfacial Rashba effect due to band bending of Cd_3As_2 beneath the FM electrode. Furthermore, the spin texture observed by nonlocal measurements is consistent with the topological surface states, indicating that Rashba spin splitting is localized on the interface between topological materials and FM metals.

II. METHODS

Cd_3As_2 is known as a topological Dirac semimetal [9] that has demonstrated many exotic physical properties, such as negative magnetoresistance [15,33,34], Berry phase π modulated Aharonov-Bohm effect [35], and Fano effect [36]. Using the chemical vapor deposition method [37], high-quality Cd_3As_2 nanoplates are obtained with a (112) surface plane (see Appendix A). The Cd_3As_2 nanoplate with a thickness of about 100 nm is transferred onto the Si substrate with a 285-nm-thick SiO_2 layer. The Ti/Au and Co electrodes are fabricated via two rounds of electron beam lithography and electron beam evaporation. The native surface oxide of the nanoplate is removed in situ by Ar^+ etching treatment before metal deposition. The optical image of a typical device is shown in Fig. 1(a), where three FM Co electrodes are denoted in blue. Among them, two detectors are Hall-type electrodes; the other detector is across the whole sample. The rest of the electrodes are all Ti/Au electrodes. A dc bias current is applied on the two Ti/Au electrodes and the voltage is measured on the Co probe with an adjacent Ti/Au electrode as a reference [Fig. 1(b)]. The magnetic field is applied parallel to the long axis of Co electrodes, in-plane perpendicular to the current direction. All measurements are carried out in a commercial Oxford cryostat. Tens of devices are fabricated and measured, demonstrating reproduceable results. Here, we report the results measured from a typical device in the main text.

The FM electrodes are used as spin detectors to directly detect spin transport and measure the spin-dependent voltage, V_S, in topological materials [3,4,16–21]. As demonstrated in Fig. 1(b), an external electric field along the k_x direction could induce net electron momentum along the $-k_x$ direction. Due to the spin-momentum locking of topological surface states, net spin polarization **S** along the k_y
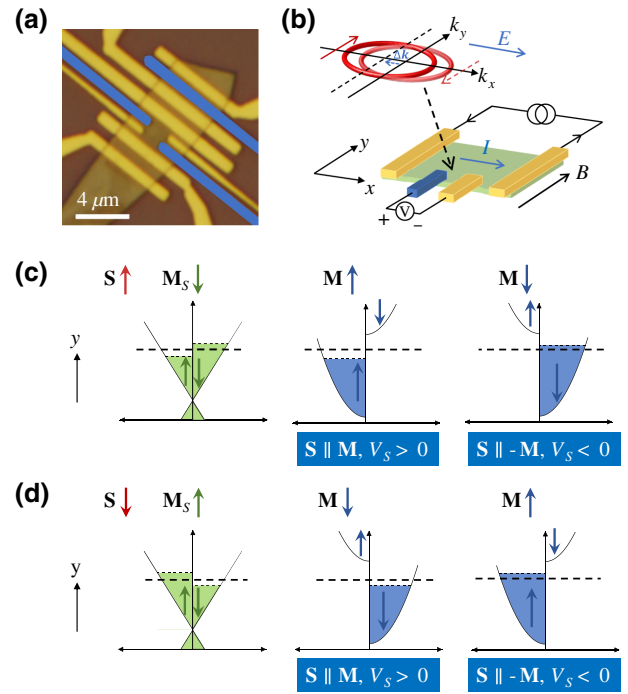

FIG. 1. Schematic of spin-transport measurements in Dirac semimetal. (a) Optical image of a typical device. Three Co electrodes are denoted in blue. Remaining electrodes are Ti/Au electrodes. (b) Illustration of spin-transport detection via Hall-type FM electrodes in topological materials. In-plane magnetic field is applied orthogonal to current direction. Inset shows the shift of Fermi surface of topological surface states and induced net spin polarization under an electric field. Illustration of the sign of the spin-dependent voltage V_S when **S** ∥ y (c) and **S** ∥ $-y$ (d). Red arrows denote the direction of spin polarization **S**. Green (blue) arrows represent the direction of Dirac semimetal magnetization M_S (FM magnetization **M**).

direction would be produced. It is worth noting that electrons possess negative charges. Thus, the magnetization of a Dirac semimetal, M_S, satisfies $M_S = -g(\mu_B/\hbar)S$ (g is the g factor, μ_B is the Bohr magneton, and $\hbar$ is the reduced Plank constant), which is antiparallel to spin polarization **S**. A spin-dependent voltage, V_S, would be obtained via the FM electrode, which is dependent on the relative directions of FM magnetization, **M**, and spin polarization, **S**. For simplicity, we assume that the FM metal is a half-metal. When **S** ∥ y, i.e., M_S ∥ $-y$, the majority subband will be occupied with electrons possessing spin moments along the $-y$ direction [left panel in Fig. 1(c)]. The electrochemical potentials of majority and minority subbands are denoted as μ_{maj} and μ_{min}, respectively. When **M** ∥ y, the electrons in the FM metal would diffuse towards the minority subband until $\mu_{FM} = \mu_{min}$, inducing a positively charged FM metal, and thus, $V_S > 0$ [middle panel in Fig. 1(c)]. On the contrary, when **M** ∥ $-y$, the electrons in the majority subband would diffuse towards the FM metal until $\mu_{FM} = \mu_{maj}$, inducing a negatively charged FM metal, and

thus, $V_S < 0$ [right panel in Fig. 1(c)]. Similar analysis can be performed for the $\mathbf{S} \parallel -y$ case, as shown in Fig. 1(d). It is found that, when the magnetization of the FM electrode $\mathbf{M}$ is parallel to $\mathbf{S}$, a positive V_S is expected [4,22], while a negative V_S would occur when $\mathbf{M} \parallel -\mathbf{S}$. The spin-dependent voltage, V_S, can be obtained after subtracting the background from raw data (see Appendix B).

III. RESULTS AND DISCUSSION

Figures 2(a) and 2(b) show the results from local spin-transport measurements via one Hall-type Co detector. Clear hysteretic loops of V_S are observed with forward and backward sweeps of the magnetic field. For bias currents of 20 and –20 μA, V_S shows inverted high (low) voltage states and counterclockwise (clockwise) hysteresis, indicating the current-polarity-controlled orientation of spin polarization. The spin orientation is always locked at right angles to the momentum k_e, showing clockwise spin helicity, which is consistent with the spin texture of topological surface states (see Appendix C). Consistent results are obtained from another Hall-type Co detector on the other side (see Appendix D).

We further investigate the gate and temperature dependence of the spin voltage, V_S, as presented in Fig. 3. From the transfer curve in Fig. 3(a), the Dirac point is found to be located at $V_g \sim -32$ V with resistance maximum. The absolute value of the loop height as a function of gate voltage is shown in Fig. 3(b). The loop height, ΔV_S, is defined as the detected voltage difference at zero magnetic field for backward and forward sweeping. It is found that $|\Delta V_S|$ shows a similar V_g dependence with resistance, demonstrating a maximum at the Dirac point. As theory proposes [22], the loop height $\Delta V_S \propto I R_B P_{\text{FM}}(\mathbf{p} \cdot \mathbf{M}_u)$, where I is the bias current, $1/R_B$ is the ballistic conductance, P_{FM} is the effective spin polarization of the FM electrode, $\mathbf{M}_u$ is the unit vector along FM magnetization, and $\mathbf{p}$ is the induced spin polarization per unit current. In Dirac semimetals, topological surface states and bulk states are always in parallel conduction. When tuning the gate voltage away from the Dirac point, the bulk-to-surface conductance ratio increases, resulting in a decrease of the

spin-polarized surface current and $|\Delta V_S|$. As shown in Figs. 3(a) and 3(b), the loop height, $|\Delta V_S|$, is reduced nearly 5 times from the Dirac point to $V_g = 30$ V, which is approximately consistent with the sixfold increase of the total conductance. Additionally, ΔV_S shows a linear dependence on bias current (see Appendix D), which is consistent with theoretical predictions [22]. The spin signal is robust against temperature [Fig. 3(c)]. Within the high-temperature regime, $|\Delta V_S|$ measured here is more significant than that measured in topological insulators with even a larger bias current (see Appendix E). The significant spin signals up to 300 K provide a promising potential for room-temperature spintronic applications based on TSMs.

Figure 4 demonstrates the spin transport measured via the Co detector that is across the whole sample. Clear hysteretic loops are observed with a bias current of $\pm 300\,\mu$A, as shown in Figs. 4(a) and 4(b), respectively. For this probe configuration, the spin direction is locked at left angles to the momentum, indicating the observed spin texture here is opposite to that of topological surface states. The Rashba spin-splitting state arising from surface band bending provides a possible origin for the opposite spin texture [4,38]. As shown in Fig. 4(c), downward band bending would occur on the surface of the Cd_3As_2 nanoplate beneath the Co electrode, where the charge-accumulation layer is formed at the interface with thickness D, leading to a strong interfacial electric field and Rashba spin splitting. Figure 4(d) illustrates the subbands and spin texture of Rashba states. Other effects that may induce this opposite spin texture in TSMs, such as local Hall effect [4,39] and trivial surface states [40], can be safely ruled out in our case (see Appendix C).

To compare the spin signals under different current bias, spin resistance is defined as $R_S = |\Delta V_S|/I$. At 1.4 K, for Hall-type Co detector, R_S equals $0.61\,\Omega$, which is an order of magnitude larger than $R_S \sim 0.036\,\Omega$ for the Co detector across the sample, further indicating that opposite spin textures indeed have different origins. Figure 4(e) shows the gate dependence of spin voltage $|\Delta V_S|$ and resistance. Different from the results via the Hall-type Co detector in Fig. 3, $|\Delta V_S|$ is insensitive to gate voltage. This may be
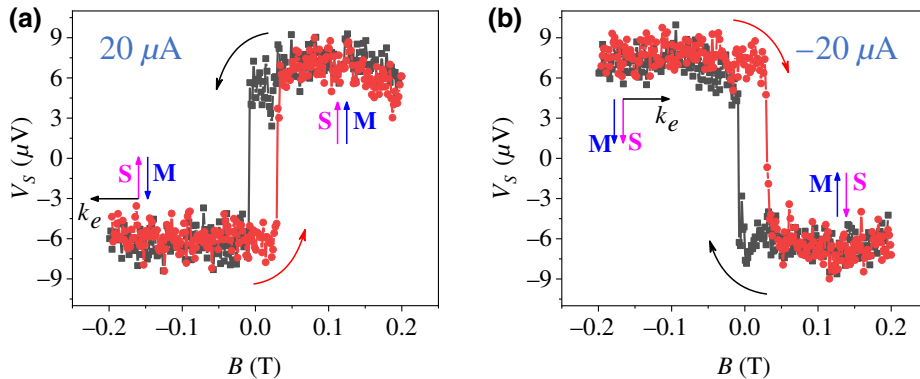

FIG. 2. Spin transport measured via Hall-type Co detector. (a),(b) Magnetic hysteretic loop of V_S via a Hall-type Co detector at 1.4 K with bias current of $\pm 20\,\mu$A, respectively.
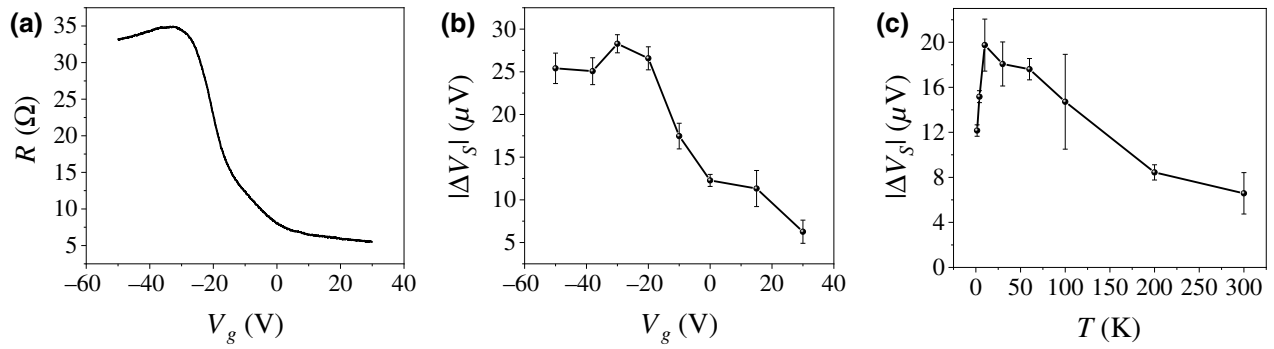
FIG. 3.   Gate and temperature dependence of spin signals. (a) Resistance as a function of gate voltage with Dirac point at $V_g = -32$ V. (b) Spin voltage V_S loop height, $|\Delta V_S|$, as a function of gate voltage, with a bias current of 20 μA. (c) $|\Delta V_S|$ as a function of temperature at a bias current of 20 μA. Error bars in (b),(c) take values of the standard deviation of multiple measurements.

because of electrostatic screening of the gate voltage from the high carrier concentration in the interfacial charge-accumulation layer. As shown in Fig. 4(f), the Rashba-type spin signal can also survive up to room temperature.

Nonlocal spin transport is further investigated via the Co detector that is across the sample. A hysteretic loop is observed with a bias current of 8 mA, as shown in Fig. 5(a). The direction of spin polarization is determined according to the high and low voltage states when **M** ∥ **S** and **M** ∥ −**S**, respectively. The charge-current-spreading effect can produce a notable nonlocal signal [41,42]. Carriers could spread within the range of the mean free path, producing a nonlocal momentum, k'_e (see Appendix F). With the determined orientations of both **S** and k'_e, the right-angle locking of spin momentum is thus obtained [inset of Fig. 5(a)], corresponding to the spin texture from

topological surface states. The nonlocal resistance, R_{NL}, and spin signal $|\Delta V_S|$ versus gate voltage are shown in Figs. 5(b) and 5(c), respectively. R_{NL} is defined as V_{NL}/I, where V_{NL} is the nonlocal voltage, while I is the local bias current. The gate dependence of both R_{NL} and $|\Delta V_S|$ show a peak feature, indicating a Dirac-type band structure. It is worth noting that the position of the Dirac point obtained via nonlocal measurements has a small shift compared with that of the local transfer curve in Fig. 4(e). This may be related to the fact that nonlocal transport is dominated by the surface states, where electrostatic screening of the gate should be significant for the approximately 100-nm-thick nanoplate [37,43].

From the observations above, we find that the measured spin texture is strongly dependent on the FM electrode configuration and local or nonlocal detection. Highly
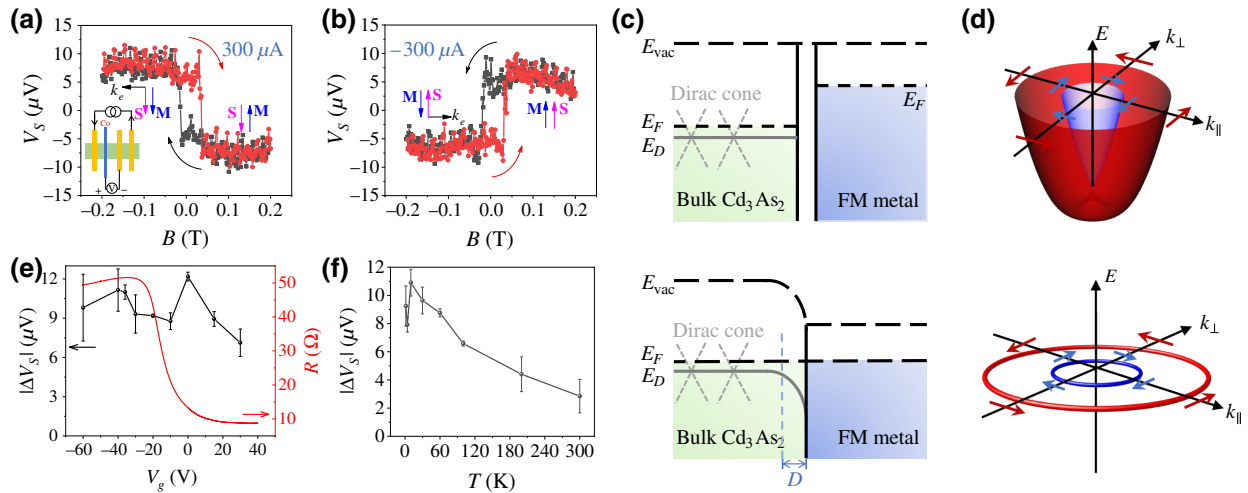

FIG. 4.   Spin detection via Co detector across the whole sample. (a),(b) Magnetic hysteretic loop at 1.4 K with bias current ± 300 μA, respectively. Inset of (a) shows the four-terminal detection configuration. (c) Energy-band diagrams of Cd_3As_2 and FM metal before (top panel) and after (bottom panel) contact. Charge-accumulation layer is formed near the interface with thickness D, as illustrated. (d) Top: Illustration of subbands with strong Rashba spin splitting. Bottom: Helical spin texture of Fermi surface of Rashba subbands. Blue and red arrows both indicate the direction of spin vector. (e) Spin-voltage loop height, $|\Delta V_S|$, and resistance versus gate voltage. (f) $|\Delta V_S|$ versus temperature. Error bars in (e),(f) take values of the standard deviation of multiple measurements.
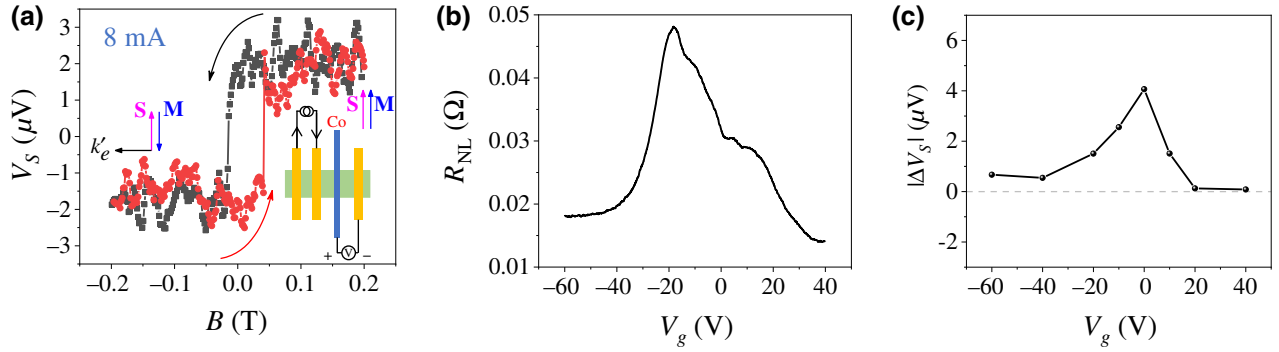
FIG. 5.   Nonlocal spin transport. (a) Nonlocal spin transport via Co detector across the whole sample at 1.4 K with bias current 8 mA. Nonlocal spin-detection configuration is illustrated in the inset. (b) Nonlocal resistance as a function of gate voltage. (c) Nonlocal spin voltage loop height, $|\Delta V_S|$, as a function of gate voltage.

consistent results are observed in different devices, that is, (1) topological surface states produced spin texture is observed via the Hall-type FM electrode, (2) a Rashba-like spin texture is observed via the FM electrode across the sample, and (3) nonlocal spin detection via the FM electrode across the sample can restore the spin texture of topological surface states. In the following, we discuss the possible mechanisms for the observations.

FM contact may greatly influence the spatial distribution of surface spin textures. Owing to the work-function difference between the FM electrode and the sample, a charge-transfer process is very common near the surface [44]. Following the prominent charge transfer, a strong interfacial electrical field is constructed, which can induce large Rashba spin splitting [4,26,45]. On the other hand, charge transfer may induce the Fermi level at the interface to be located in the bulk conduction band, far away from the Dirac point, suppressing the contribution from topological surface states. Thus, in our case, the Rashba spin texture is dominant beneath the FM electrode. The Rashba spin splitting can be eliminated by weakening the interaction between the FM electrode and sample. For example, even with the FM electrode across the sample, the Dirac semimetal with a tunneling barrier on the surface recalls the spin texture from topological surface states [12].

It is worth noting that an effective external electric field applied on the sample region with specified spin texture is necessary to produce the spin-polarized current, that is, the Edelstein effect. For the FM detector across the sample, the detected region is completely covered by the FM electrode and there must be an effective electric field in this region under an applied bias. By comparison, for the Hall-type electrode, the detected region contains not only the small contacting region with the FM detector, but also the surface that is not covered by the electrode. Near this region, transport conduction should be dominated by the topological surface states, and thus, spin polarization from the topological spin texture can be detected. For nonlocal measurements, although the Rashba-type spin texture may

still exist beneath the FM electrode, the external electric field exerted on this nonlocal region is nearly zero. The nonlocal FM electrode just serves as a spin detector. Thus, the spin-polarized surface states with topological protection and a long mean free path [6,12] coming from the source-drain region can be detected nonlocally.

IV. CONCLUSION

We demonstrate the control of spin texture by designing different electrode patterns in Dirac semimetal Cd_3As_2 nanoplates. Hall-type Co electrodes facilitate the spin texture from topological surface states, while Co electrodes across the whole sample manifest the opposite spin polarization, which provides guidance for the design of high-efficiency SOT devices based on topological materials [30,45,46]. By patterning the FM electrodes into different configurations, opposite spin polarizations are induced, even at room temperature in different regions of a single device. Our results indicate that the interaction between the FM and topological material plays an important role on the spin texture and an optimized pattern design can help to pick out the spin with a specific orientation.

APPENDIX A: CHARACTERIZATION OF THE SYNTHESIZED CADMIUM ARSENIDE NANOPLATES

High-quality Cd_3As_2 nanoplates in our work are grown via the chemical vapor deposition method, as mentioned in our previous work [37]. Figure 6(a) shows a scanning electron microscopy (SEM) image of the
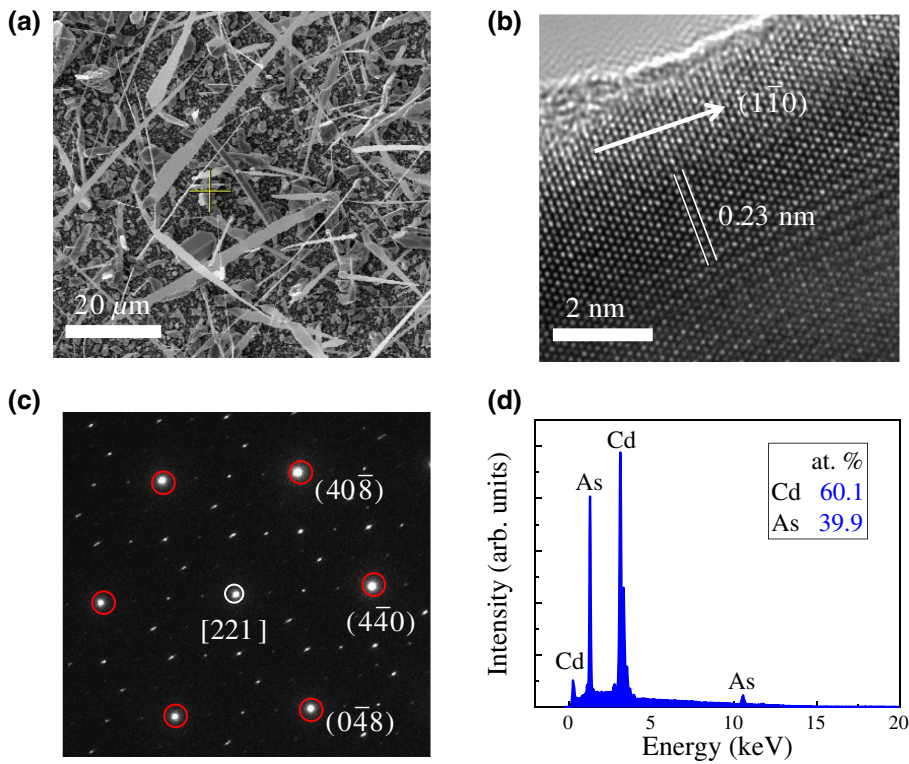
FIG. 6. (a) SEM image of nanoplates. (b) High-resolution TEM image of a typical nanoplate with an interplanar spacing of about 0.23 nm, indicating the $(1\bar{1}0)$ edge direction. (c) Corresponding SAED pattern demonstrates the [221] zone axis, indicating that the naturally grown surface is (112) plane. (d) EDS spectrum of a single nanoplate. Qualitative analysis suggests the atomic ratio of Cd to As is nearly 3:2.

synthesized nanoplates. The high-resolution transmission electron microscopy (TEM) image shows an interplanar spacing of about 0.23 nm, indicating the $(1\bar{1}0)$ edge direction of the nanoplate [Fig. 6(b)]. The selected-area electron diffraction (SAED) pattern is shown in Fig. 6(c). Besides the central point, there are six diffraction points, whose intensities are much larger than those of the other points. After calculating the distances from each diffraction point to the central point and their relative orientations, we can determine the $(40\bar{8})$, $(4\bar{4}0)$, and $(0\bar{4}8)$ crystal planes, as highlighted in Fig. 6(c). Then, we can determine the [221] zone axis based on crystallography calculations, which indicate that the naturally grown surface of the nanoplate is the (112) plane. Qualitative analysis of the energy-dispersive x-ray spectroscopy (EDS) results suggests that the atomic ratio of Cd to As is 60.1:39.9, which

is approximately consistent with the chemical composition of Cd_3As_2 [Fig. 6(d)].

APPENDIX B: RAW DATA OF MAGNETIC HYSTERETIC LOOPS

Since the bulk states of Dirac semimetals are also conducting, the measured voltage, V, contains not only the spin-dependent voltage, V_S, but also a spin-independent background, V_B. We show raw data corresponding to Figs. 2(a) and 2(b) in Figs. 7(a) and 7(b). V_B is a linear background, as denoted by dotted lines. V_S is obtained by removing V_B from raw data, i.e., $V_S = V - V_B$. Background subtraction is a very common method in spin potentiometric measurements [3,17].
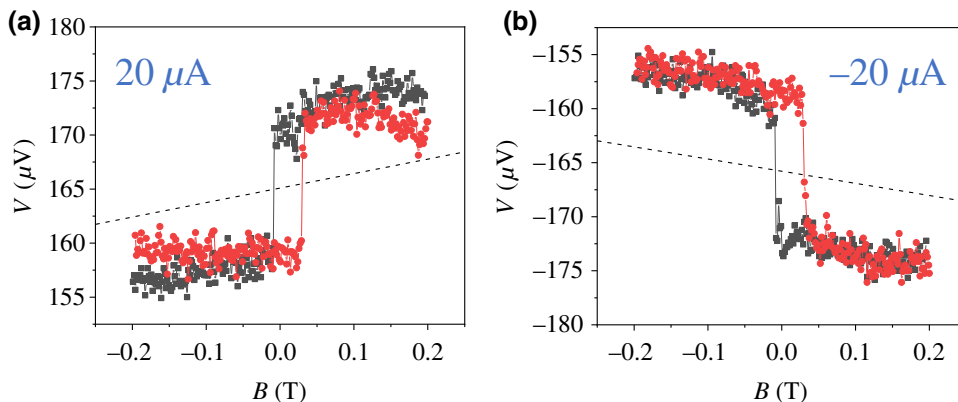

FIG. 7. (a),(b) Raw data corresponding to Figs. 2(a) and 2(b) of main text, respectively. Background is denoted by dotted lines.
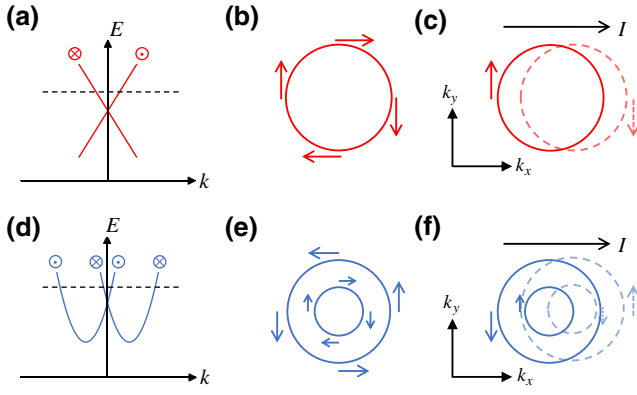
FIG. 8. (a),(d) Illustration of the topological surface and Rashba states, respectively. (b),(e) Constant energy contour of bands for topological surface and Rashba states, respectively. (c),(f) Illustration of current-induced spin polarization for topological surface and Rashba states, respectively. Arrows denote the direction of spin vector.

APPENDIX C: CURRENT-INDUCED SPIN POLARIZATION FOR TOPOLOGICAL SURFACE STATES AND RASHBA STATES

Topological surface states and Rashba states usually possess opposite spin textures, as shown in Figs. 8(b) and 8(e). When applying the same bias current along the $+x$ direction [Figs. 8(c) and 8(f)], the Fermi surface would be

shifted towards the $-k_x$ direction and induce net electron momentum, k_e, along the $-k_x$ direction. Due to spin-momentum locking, net spin polarization is expected. For topological surface states [Figs. 8(a)–8(c)], the induced spin polarization is along the k_y direction, while, for Rashba states [Figs. 8(d)–8(f)], the induced spin polarization is along the $-k_y$ direction.

Thus, through spin potentiometric measurements, we can identify the helicity of the spin texture by the polarity of the loop. If the spin polarization, **S**, is locked at right angles to k_e, the spin signal comes from topological surface states. Otherwise, the spin signal could be attributed to Rashba states.

The observed spin texture with counterclockwise helicity most likely originates from the Rashba spin-splitting effect of two-dimensional electron gas near the interfaces. Other effects that may induce such a spin texture in TSMs can be safely ruled out in our case. For the local Hall effect [39], the polarity of the voltage loop is random, which is inconsistent with our results. Additionally, intrinsic surface states in TSMs can also demonstrate a Rashba-like spin texture [40]. Sometimes the lower branch surface states may overlap with the upper branch near the Fermi level with opposite spin texture, inducing a Rashba-like spin texture. However, this explanation is inconsistent with the gate dependence investigations. If the Rashba-like spin texture originates from lower branch surface states, it should be sensitive to gate voltages, since the gate can
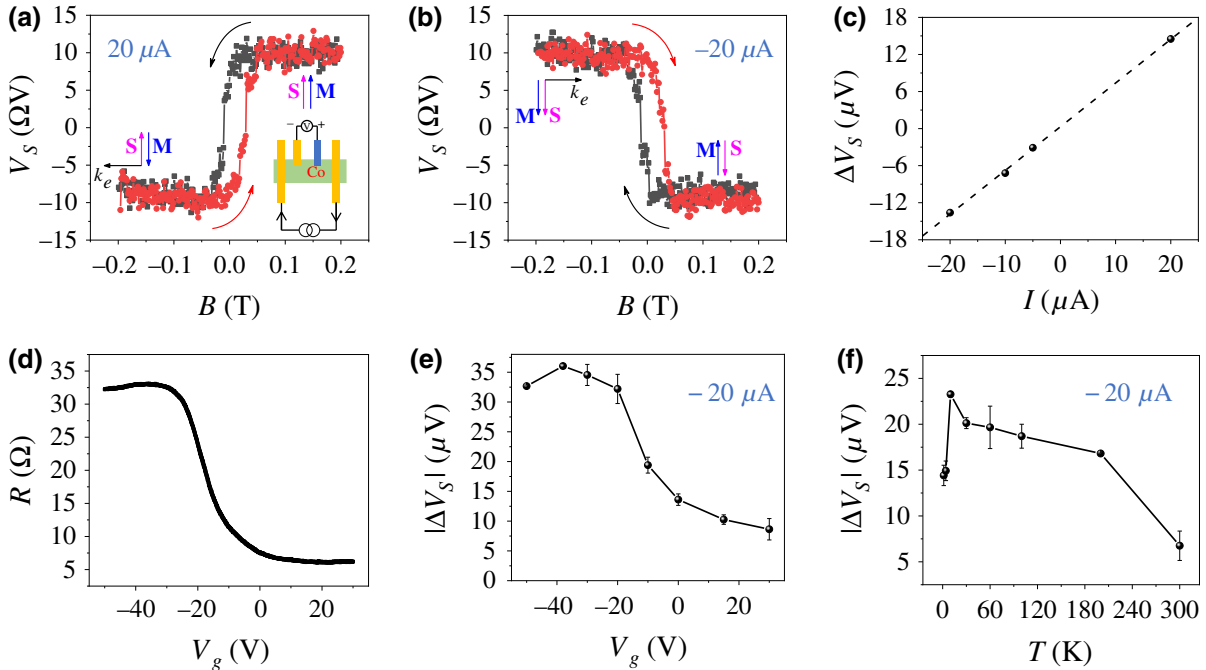

FIG. 9. (a),(b) Magnetic hysteretic loop at 1.4 K with bias current $\pm 20\,\mu$A, respectively. Local spin-detection configuration is shown in the inset of (a). (c) Spin loop height, ΔV_S, as a function of bias current at 1.4 K. (d),(e) Resistance and spin loop height, $|\Delta V_S|$, as a function of gate voltage for a bias current of $-20\,\mu$A. (f) $|\Delta V_S|$ as a function of temperature for a bias current of $-20\,\mu$A. Error bars in (e),(f) take values of the standard deviation of multiple measurements.
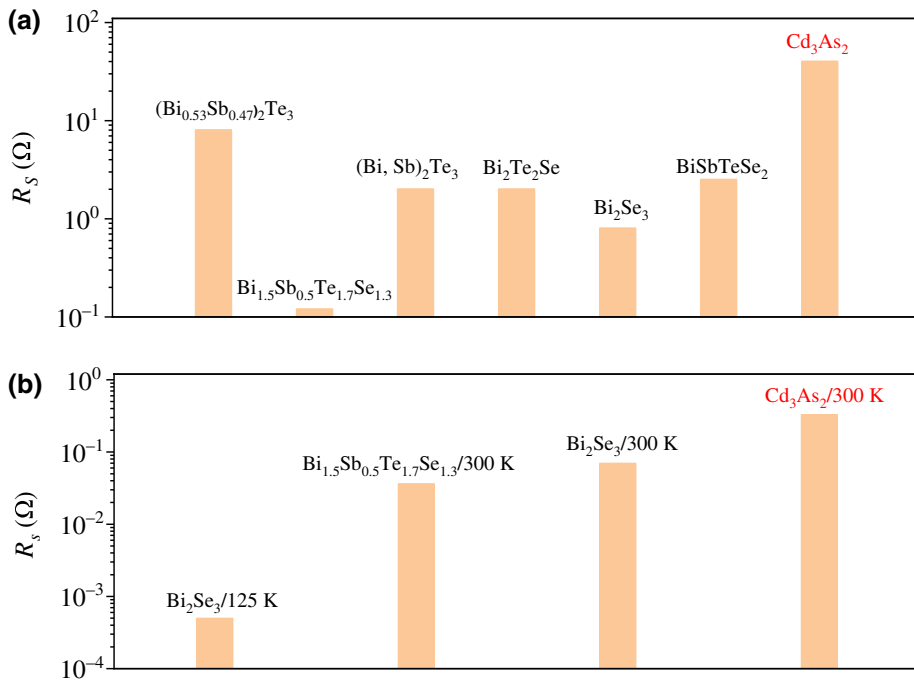
FIG. 10. (a) Data are collected from $(Bi_{0.53}Sb_{0.47})_2Te_3$ at 1.9 K (Ref. [16]), $Bi_{1.5}Sb_{0.5}Te_{1.7}Se_{1.3}$ at 4.2 K (Ref. [18]), $(Bi, Sb)_2Te_3$ at 1.8 K (Ref. [20]), Bi_2Te_2Se at 1.6 K (Ref. [21]), Bi_2Se_3 at 1.4 K (Ref. [23]), $BiSbTeSe_2$ at 2 K (Ref. [24]), and Cd_3As_2 at 2 K (Ref. [12]). (b) Data are collected from Bi_2Se_3 at 125 K (Ref. [3]), $Bi_{1.5}Sb_{0.5}Te_{1.7}Se_{1.3}$ at 300 K (Ref. [18]), Bi_2Se_3 at 300 K (Ref. [17]), and Cd_3As_2 at 300 K (this work).

effectively tune the Fermi level. Nevertheless, the observed Rashba-type spin signal is almost unchanged, even when the Fermi level is tuned far away from the Dirac point.

APPENDIX D: LOCAL SPIN TRANSPORT VIA ANOTHER HALL-TYPE FM ELECTRODE

Figure 9 demonstrates the local spin-transport measurements via another Hall-type Co electrode in the same device as that in Fig. 2. As shown in Figs. 9(a) and 9(b), the spin polarization is locked at right angles to electron momentum, which is consistent with the spin texture of topological surface states. The spin loop height, ΔV_S, is found to be linearly dependent on bias current [Fig. 9(c)], in accordance with theoretical expectations [22]. The spin resistance is estimated to be $R_S \sim 0.71$ Ω, which is similar to $R_S \sim 0.61$ Ω presented in Fig. 2. As shown in Figs. 9(d) and 9(e), the spin loop height, $|\Delta V_S|$, has a similar dependence on gate voltage as that of the resistance, indicating that the gate can effectively tune the bulk-to-surface conductance ratio, which affects the ratio of the spin signal

to the total signal. Interestingly, the spin signal is robust against temperature, which can survive up to room temperature [Fig. 9(f)] and is beneficial for room-temperature spintronic applications.

APPENDIX E: COMPARISON OF SPIN RESISTANCE R_S BETWEEN TOPOLOGICAL INSULATOR AND DIRAC SEMIMETAL

We define spin resistance, R_S, as $R_S \equiv |\Delta V_S/I|$, where ΔV_S is the spin voltage loop height and I is the applied bias current. The spin resistance can be used to characterize the charge-to-spin conversion efficiency. Figure 10 shows a comparison of spin resistance, R_S, between topological insulators and the Dirac semimetal Cd_3As_2. Compared with topological insulator materials, the Dirac semimetal Cd_3As_2 demonstrates a larger spin resistance in both low- and high-temperature regimes, which is promising for practical and high-performance spintronic applications.
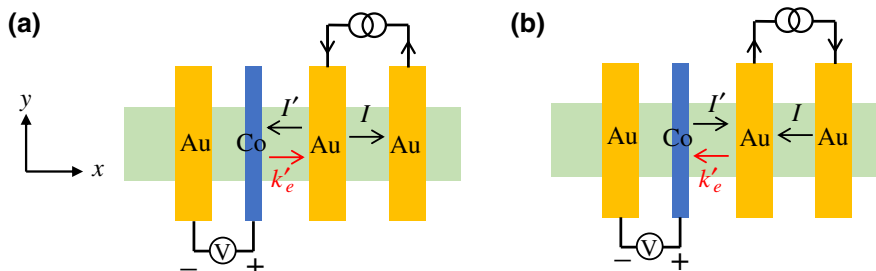

FIG. 11. Nonlocal transport induced by charge-current-spreading (CCS) effect. I denotes local current, while I' denotes nonlocal current.

APPENDIX F: MECHANISM OF NONLOCAL SPIN TRANSPORT

In nonlocal transport, the CCS effect is universally observed. The CCS effect is similar to the concept of current leakage. Current can flow towards the region with low electric potentials. As shown in Fig. 11(a), when the local current is along the $+x$ axis, the electric potential of the local Au electrode adjacent the nonlocal region is high, inducing a nonlocal current along the $-x$ direction. Otherwise, when the local current is along the $-x$ axis [Fig. 11(b)], the electric potential of the local Au electrode adjacent the nonlocal region is low, inducing a nonlocal current along the $+x$ direction. Thus, for the CCS effect, when the local current is reversed, the nonlocal current, and thus, nonlocal electron momentum, k'_e, would reverse the signs. In the CCS regime, the nonlocal current flows between the local and nonlocal electrode within the scale of the electron mean free path. In our devices, the distance between the nonlocal FM electrode and adjacent local Au electrode is set to 500 nm, which is much larger than the mean free path of bulk electrons. Thus, the detected nonlocal signals mainly originate from the CCS effect of topological surface states.

---

[1] X.-L. Qi and S.-C. Zhang, Topological insulators and superconductors, Rev. Mod. Phys. **83,** 1057 (2011).

[2] M. Z. Hasan and C. L. Kane, Colloquium: Topological insulators, Rev. Mod. Phys. **82,** 3045 (2010).

[3] C. H. Li, O. M. J. van 't Erve, J. T. Robinson, Y. Liu, L. Li, and B. T. Jonker, Electrical detection of charge-current-induced spin polarization due to spin-momentum locking in Bi_2Se_3, Nat. Nanotechnol. **9,** 218 (2014).

[4] F. Yang, S. Ghatak, A. A. Taskin, K. Segawa, Y. Ando, M. Shiraishi, Y. Kanai, K. Matsumoto, A. Rosch, and Y. Ando, Switching of charge-current-induced spin polarization in the topological insulator $BiSbTeSe_2$, Phys. Rev. B **94,** 075304 (2016).

[5] I. Žutić, J. Fabian, and S. Das Sarma, Spintronics: Fundamentals and applications, Rev. Mod. Phys. **76,** 323 (2004).

[6] A.-Q. Wang, X.-G. Ye, D.-P. Yu, and Z.-M. Liao, Topological semimetal nanostructures: From properties to topotronics, ACS Nano **14,** 3755 (2020).

[7] X. Wan, A. M. Turner, A. Vishwanath, and S. Y. Savrasov, Topological semimetal and Fermi-arc surface states in the electronic structure of pyrochlore iridates, Phys. Rev. B **83,** 205101 (2011).

[8] Z. Wang, Y. Sun, X.-Q. Chen, C. Franchini, G. Xu, H. Weng, X. Dai, and Z. Fang, Dirac semimetal and topological phase transitions in A_3Bi ($A = $ Na, K, Rb), Phys. Rev. B **85,** 195320 (2012).

[9] Z. Wang, H. Weng, Q. Wu, X. Dai, and Z. Fang, Three-dimensional Dirac semimetal and quantum transport in Cd_3As_2, Phys. Rev. B **88,** 125427 (2013).

[10] N. P. Armitage, E. J. Mele, and A. Vishwanath, Weyl and Dirac semimetals in three-dimensional solids, Rev. Mod. Phys. **90,** 015001 (2018).

[11] S.-Y. Xu, I. Belopolski, D. S. Sanchez, M. Neupane, G. Chang, K. Yaji, Z. Yuan, C. Zhang, K. Kuroda, G. Bian, et al., Spin Polarization and Texture of the Fermi Arcs in the Weyl Fermion Semimetal TaAs, Phys. Rev. Lett. **116,** 096801 (2016).

[12] B.-C. Lin, S. Wang, A.-Q. Wang, Y. Li, R.-R. Li, K. Xia, D. Yu, and Z.-M. Liao, Electric Control of Fermi Arc Spin Transport in Individual Topological Semimetal Nanowires, Phys. Rev. Lett. **124,** 116802 (2020).

[13] H. Yi, Z. Wang, C. Chen, Y. Shi, Y. Feng, A. Liang, Z. Xie, S. He, J. He, Y. Peng, et al., Evidence of topological surface state in three-dimensional Dirac semimetal Cd_3As_2, Sci. Rep. **4,** 6106 (2014).

[14] T. Liang, Q. Gibson, M. N. Ali, M. Liu, R. J. Cava, and N. P. Ong, Ultrahigh mobility and giant magnetoresistance in the Dirac semimetal Cd_3As_2, Nat. Mater. **14,** 280 (2015).

[15] C.-Z. Li, L.-X. Wang, H. Liu, J. Wang, Z.-M. Liao, and D.-P. Yu, Giant negative magnetoresistance induced by the chiral anomaly in individual Cd_3As_2 nanowires, Nat. Commun. **6,** 10137 (2015).

[16] J. Tang, L.-T. Chang, X. Kou, K. Murata, E. S. Choi, M. Lang, Y. Fan, Y. Jiang, M. Montazeri, W. Jiang, et al., Electrical detection of spin-polarized surface states conduction in $(Bi_{0.53}Sb_{0.47})_2Te_3$ topological insulator, Nano Lett. **14,** 5423 (2014).

[17] A. Dankert, J. Geurs, M. V. Kamalakar, S. Charpentier, and S. P. Dash, Room temperature electrical detection of spin polarized currents in topological insulators, Nano Lett. **15,** 7976 (2015).

[18] Y. Ando, T. Hamasaki, T. Kurokawa, K. Ichiba, F. Yang, M. Novak, S. Sasaki, K. Segawa, Y. Ando, and M. Shiraishi, Electrical detection of the spin polarization due to charge flow in the surface state of the topological insulator $Bi_{1.5}Sb_{0.5}Te_{1.7}Se_{1.3}$, Nano Lett. **14,** 6226 (2014).

[19] L. Liu, A. Richardella, I. Garate, Y. Zhu, N. Samarth, and C.-T. Chen, Spin-polarized tunneling study of spin-momentum locking in topological insulators, Phys. Rev. B **91,** 235437 (2015).

[20] J. S. Lee, A. Richardella, D. R. Hickey, K. A. Mkhoyan, and N. Samarth, Mapping the chemical potential dependence of current-induced spin polarization in a topological insulator, Phys. Rev. B **92,** 155312 (2015).

[21] J. Tian, I. Miotkowski, S. Hong, and Y. P. Chen, Electrical injection and detection of spin-polarized currents in topological insulator Bi_2Te_2Se, Sci. Rep. **5,** 14293 (2015).

[22] S. Hong, V. Diep, S. Datta, and Y. P. Chen, Modeling potentiometric measurements in topological insulators including parallel channels, Phys. Rev. B **86,** 085131 (2012).

[23] J. Tian, I. Childres, H. Cao, T. Shen, I. Miotkowski, and Y. P. Chen, Topological insulator based spin valve devices: Evidence for spin polarized transport of spin-momentum-locked topological surface states, Solid State Commun. **191,** 1 (2014).

[24] M. Zhang, X. Wang, S. Zhang, Y. Gao, Z. Yu, X. Zhang, M. Gao, F. Song, J. Du, X. Wang, et al., Unique current-direction-dependent ON–OFF switching in $BiSbTeSe_2$ topological insulator-based spin valve transistors, IEEE Electron Device Lett. **37,** 1231 (2016).

[25] O. V. Yazyev, J. E. Moore, and S. G. Louie, Spin Polarization and Transport of Surface States in the Topological

Insulators Bi_2Se_3 and Bi_2Te_3 From First Principles, Phys. Rev. Lett. **105**, 266806 (2010).

[26] Z. H. Zhu, G. Levy, B. Ludbrook, C. N. Veenstra, J. A. Rosen, R. Comin, D. Wong, P. Dosanjh, A. Ubaldini, P. Syers, et al., Rashba Spin-Splitting Control at the Surface of the Topological Insulator Bi_2Se_3, Phys. Rev. Lett. **107**, 186405 (2011).

[27] Y. Shiomi, K. Nomura, Y. Kajiwara, K. Eto, M. Novak, K. Segawa, Y. Ando, and E. Saitoh, Spin-Electricity Conversion Induced by Spin Injection Into Topological Insulators, Phys. Rev. Lett. **113**, 196601 (2014).

[28] Y. Fan, P. Upadhyaya, X. Kou, M. Lang, S. Takei, Z. Wang, J. Tang, L. He, L.-T. Chang, M. Montazeri, et al., Magnetization switching through giant spin–orbit torque in a magnetically doped topological insulator heterostructure, Nat. Mater. **13**, 699 (2014).

[29] Y. Wang, P. Deorani, K. Banerjee, N. Koirala, M. Brahlek, S. Oh, and H. Yang, Topological Surface States Originated Spin-Orbit Torques in Bi_2Se_3, Phys. Rev. Lett. **114**, 257202 (2015).

[30] J. Han, A. Richardella, S. A. Siddiqui, J. Finley, N. Samarth, and L. Liu, Room-Temperature spin-orbit torque switching induced by a topological insulator, Phys. Rev. Lett **119**, 077702 (2017).

[31] Y. Wang, D. Zhu, Y. Wu, Y. Yang, J. Yu, R. Ramaswamy, R. Mishra, S. Shi, M. Elyasi, K.-L. Teo, et al., Room temperature magnetization switching in topological insulator-ferromagnet heterostructures by spin-orbit torques, Nat. Commun. **8**, 1364 (2017).

[32] A. R. Mellnik, J. S. Lee, A. Richardella, J. L. Grab, P. J. Mintun, M. H. Fischer, A. Vaezi, A. Manchon, E. A. Kim, N. Samarth, et al., Spin-transfer torque generated by a topological insulator, Nature **511**, 449 (2014).

[33] H. Li, H. He, H.-Z. Lu, H. Zhang, H. Liu, R. Ma, Z. Fan, S.-Q. Shen, and J. Wang, Negative magnetoresistance in Dirac semimetal Cd_3As_2, Nat. Commun. **7**, 10301 (2016).

[34] C. Zhang, E. Zhang, W. Wang, Y. Liu, Z.-G. Chen, S. Lu, S. Liang, J. Cao, X. Yuan, L. Tang, et al., Room-temperature chiral charge pumping in Dirac semimetals, Nat. Commun. **8**, 13741 (2017).

[35] L.-X. Wang, C.-Z. Li, D.-P. Yu, and Z.-M. Liao, Aharonov–Bohm oscillations in Dirac semimetal Cd_3As_2 nanowires, Nat. Commun. **7**, 10769 (2016).

[36] S. Wang, B.-C. Lin, W.-Z. Zheng, D. Yu, and Z.-M. Liao, Fano Interference Between Bulk and Surface States of a Dirac Semimetal Cd_3As_2 Nanowire, Phys. Rev. Lett. **120**, 257701 (2018).

[37] C.-Z. Li, J.-G. Li, L.-X. Wang, L. Zhang, J.-M. Zhang, D. Yu, and Z.-M. Liao, Two-carrier transport induced hall anomaly and large tunable magnetoresistance in Dirac semimetal Cd_3As_2 nanoplates, ACS Nano **10**, 6020 (2016).

[38] A. Manchon, H. C. Koo, J. Nitta, S. M. Frolov, and R. A. Duine, New perspectives for Rashba spin–orbit coupling, Nat. Mater. **14**, 871 (2015).

[39] E. K. de Vries, A. M. Kamerbeek, N. Koirala, M. Brahlek, M. Salehi, S. Oh, B. J. van Wees, and T. Banerjee, Towards the understanding of the origin of charge-current-induced spin voltage signals in the topological insulator Bi_2Se_3, Phys. Rev. B **92**, 201102 (2015).

[40] A. Soumyanarayanan and J. E. Hoffman, Momentum-resolved STM studies of Rashba-split surface states on the topological semimetal Sb, J. Electron Spectrosc. Relat. Phenom. **201**, 66 (2015).

[41] T.-H. Hwang, H.-S. Kim, H. Kim, J. S. Kim, and Y.-J. Doh, Electrical detection of spin-polarized current in topological insulator $Bi_{1.5}Sb_{0.5}Te_{1.7}Se_{1.3}$, Curr. Appl. Phys. **19**, 917 (2019).

[42] J. Hu, G. Stecklein, D. A. Deen, Q. Su, P. A. Crowell, and S. J. Koester, Scaling of the nonlocal spin and baseline resistances in graphene lateral spin valves, IEEE Trans. Electron Devices **66**, 5003 (2019).

[43] C.-Z. Li, C. Li, L.-X. Wang, S. Wang, Z.-M. Liao, A. Brinkman, and D.-P. Yu, Bulk and surface states carried supercurrent in ballistic Nb-Dirac semimetal Cd_3As_2 nanowire-Nb junctions, Phys. Rev. B **97**, 115446 (2018).

[44] Z. Zhang and J. T. Yates, Band bending in semiconductors: Chemical and physical consequences at surfaces and interfaces, Chem. Rev. **112**, 5520 (2012).

[45] P. B. Ndiaye, C. A. Akosa, M. H. Fischer, A. Vaezi, E. A. Kim, and A. Manchon, Dirac spin-orbit torques and charge pumping at the surface of topological insulators, Phys. Rev. B **96**, 014408 (2017).

[46] K. Kondou, R. Yoshimi, A. Tsukazaki, Y. Fukuma, J. Matsuno, K. S. Takahashi, M. Kawasaki, Y. Tokura, and Y. Otani, Fermi-level-dependent charge-to-spin current conversion by Dirac surface states of topological insulators, Nat. Phys. **12**, 1027 (2016).